ACS APPLIED MATERIALS & INTERFACES

www.acsami.org

Research Article

Atmospheric Pressure and Ambient Temperature Plasma Jet Sintering of Aerosol Jet Printed Silver Nanoparticles

Nazli Turan,[§] Mortaza Saeidi-Javash,[§] Jiahao Chen, Minxiang Zeng, Yanliang Zhang,* and David B. Go*

Cite This: https://doi.org/10.1021/acsami.1c14049

Read Online

ACCESS | Metrics & More | Article Recommendations | Supporting Information

ABSTRACT: Atmospheric pressure nonthermal plasmas hold great promise for applications in environmental control, energy conversion, and material processing. Even at room temperature, nonthermal plasmas produce energetic and reactive species that can initiate surface modifications at a plasma−surface interface, including thin-film nanoparticle assemblies, in a nondestructive and effective way. Here, we present the plasma-activated sintering of aerosol jet printed silver thin films on substrates ranging from glass to delicate materials including blotting paper, fruits, and flexible plastic. We characterize the microstructural evolutions and electrical properties of printed films along with the electrical, thermal, and optical properties of an argon plasma jet. We demonstrate an electrical conductivity as high as 1.4 × 10^6 S/m for printed films sintered under atmospheric conditions in which the surface temperature stays below 50 °C. These results highlight a future direction where additive manufacturing of electronic devices can be achieved on flexible and low-melting-point materials under ambient conditions without requiring additional thermal processing by utilizing nonthermal plasmas.

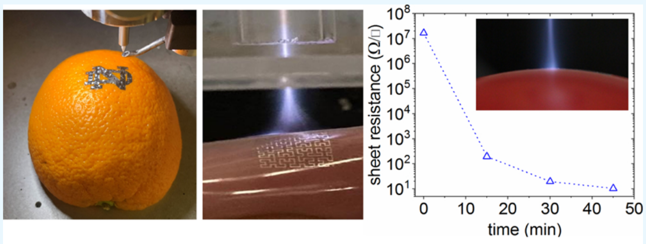

Plasma sintering on delicate materials

KEYWORDS: *plasma jet sintering, atmospheric pressure, low temperature, flexible electronics, aerosol jet printing*

1. INTRODUCTION

In the past decade, interest has surged in developing materials and techniques for manufacturing flexible electronics. Traditional methods such as photolithography and vacuum deposition require expensive equipment, include multistage processes, and are incompatible with the fabrication of devices on conformal surfaces. Additive manufacturing of flexible electronics using screen printing, inkjet printing, and aerosol jet printing (AJP) has received tremendous interest due to its low cost, rapid processing capability, and high efficiency.[1−3] AJP, in particular, has been implemented to fabricate a large variety of electronic devices using a wide range of nanoparticle (NP)-based inks, including metals, semiconductors, and dielectrics, on conformal surfaces.[4,5] In this method, the printable ink is first aerosolized using a pneumatic or ultrasonic atomizer, and the aerosol is then aerodynamically focused by a sheath gas through a fine nozzle and deposited onto a substrate. AJP enables printing functional NPs and dispersants with a feature size as small as 10 μm.

Achieving a densified, continuous film of printed NPs typically requires thermal sintering at temperatures higher than 200 °C for several hours, where the elevated temperature leads both to the removal of solvents/surfactants and enables the NPs to diffuse and consolidate, resulting in films with improved mechanical, thermal, and electrical transport properties.[6−8] The removal temperature of typical stabilizing agents [e.g., polyvinyl chloride (PVC)] ranges from 100 to 260 °C,[9] and to achieve sintering, the temperature needs to be elevated above this range. For printing flexible and wearable electronics, exploiting flexible/stretchable substrates with low melting temperatures [e.g., fabrics and plastics such as polyethylene terephthalate (PET) and polyethylene naphthalate (PEN)] is necessary. Therefore, a method enabling both the removal of surfactants and sintering at near ambient temperatures presents a technological need.

Recently developed sintering methods including laser sintering, photonic sintering, and plasma sintering have been implemented to meet the requirements of fast and roll-to-roll manufacturing of functional thin films.[4,10,11] Spark plasma sintering (SPS) has been the most common plasma-based sintering technique and is well-recognized for being rapid, combining high pressure and high current, and activation by energetic plasma species.[12−22] However, this technique utilizes a plasma spark, where the plasma is thermalized (i.e., in equilibrium) and thus acts primarily as a heating source, leading to a rapid increase in system temperature.

Received: July 28, 2021
Accepted: September 10, 2021

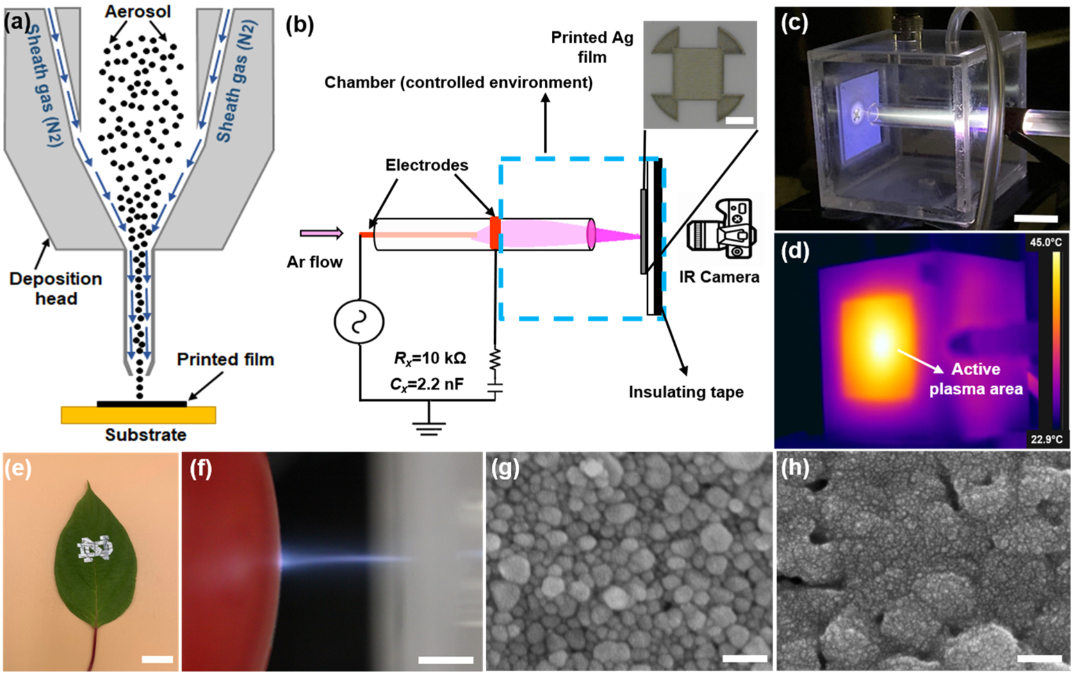

Figure 1. Atmospheric pressure and low-temperature plasma sintering of aerosol jet printed silver NP films. (a) Schematic illustration of the deposition head of the aerosol jet printer. (b) Schematic illustration of the plasma sintering setup. (c) Photograph of plasma jet impinging on PEL paper. The scale bar is 10 mm. (d) IR camera image of the test chamber showing temperature distribution during plasma exposure. (e) Aerosol jet printed Notre Dame logo (ND) on a leaf. The scale bar is 1 cm. (f) Argon plasma jet sintering of the printed Ag NP film on a tomato. The scale bar is 5 mm. (g,h) Top-view SEM images of the printed silver NP films before (g) and after (h) plasma sintering for 100 min. The scale bar is 50 nm.

Nonthermal plasmas are an alternative plasma regime characterized by nonequilibrium, where the electrons are energetic (~1−10 eV or ~10,000 K), but the ions and surrounding gas are much colder and can even stay around ambient temperature.[23,24] They offer an attractive alternative to SPS because they can overcome the temperature restrictions required of delicate and flexible materials. In this case, low-temperature sintering is presumed to be driven by energetic plasma species mobilizing the surfaces of NPs rather than a heating effect. Low pressure nonthermal plasma sintering has been implemented in vacuum chambers with pressures of 0.1−2000 mTorr and with powers of 10−900 W using radio frequency (rf) plasmas.[25−27] Others have demonstrated atmospheric pressure plasma sintering utilizing rf-powered electrodes or plasma jets with heated plates (<150 °C) and obtain electrical conductivities close to bulk values.[6,28,29]

Near-room-temperature (~60 °C) chemical sintering of silver (Ag) NPs has been proven effective depending on major factors such as NP size, the amount of surfactant, sintering temperature, and film morphology.[30] Studies have also showed that sintering is even possible at room temperature with the presence of charged photoelectrolytes and chloride ions,[31,32] while others have demonstrated that aqueous Ag NP inks can be utilized to obtain conductive films by drying for 24 h in air at room temperature.[33] These studies demonstrated electrical conductivities on the order of 10^7 S/m, which is similar to conductivities achieved with the various aforementioned plasma sintering methods. The advantage of utilizing plasma systems in sintering is their adaptability for high quantity processing without requiring synthesizing or washing steps to adjust a specific amount of chemicals and solvents.

Here, we present a plasma jet processing method for sintering aerosol jet printed silver NPs at temperatures suitable for delicate substrates including papers and fruits. A plasma jet is composed of flow-guided ionization waves that are weakly ionized, highly reactive, and low temperature, suitable for interacting with sensitive surfaces.[34−39] Plasma jets have been used extensively for tissue engineering and wound healing[40−42] and for treatment of liquids.[43−45] The propagation and electrical characterization of plasma jets have been studied and well-described in the literature.[46−49] Therefore, fundamental knowledge of plasma jets can easily be adapted for sintering within the context of plasma−surface interactions.

In this work, we demonstrate the capability of atmospheric pressure, ambient temperature plasma jets to sinter printed Ag NPs without the need for external pressurizing equipment, vacuum chambers, or heating sources. Our studies show that the substrate temperature can be maintained below 50 °C throughout the process by applying the plasma periodically (on/off). With a deposited power of 12 W during the on period and a total sintering time of 100 min, we achieve an electrical conductivity of 1.1 × 10^6 S/m for printed films on glass. Moreover, sintering of the printed films on PEL blotting paper produced an electrical conductivity of 1.4 × 10^6 S/m using a plasma power of only 6 W, implying improved energy transfer from plasma species to a film printed on porous paper. Finally, we also demonstrate sintering on delicate substrates including the flesh of a ripe tomato, a leaf, and flexible plastic, with no apparent damage. These results reveal the potential for atmospheric pressure and low temperature sintering for printed flexible electronics.

2. RESULTS AND DISCUSSION

Colloidal silver NP inks were printed using the AJP technique. Silver ink with 30−50 nm particles was printed on various substrates (Figure 1a), including glass (~1 mm thick) and PEL P60 blotting paper (~0.1 mm). After printing, the films were sintered with a plasma jet and the electrical conductivity of the sintered films was measured using the van der Pauw method (details in the Experimental Section).

The plasma sintering apparatus consisted of a plasma jet that operates in a cylindrical volume dielectric barrier discharge configuration using a quartz tube, with an external concentric copper tape as a ground electrode and a 1.2 mm diameter axially centered stainless-steel rod inside the tube as a powered electrode (Figure 1b). To form the plasma jet, argon (Ar) was flowed through the quartz tube at 1500 mL/min into a continuously filled (10 mL/min) nitrogen (N_2) cubic plexiglass chamber (40 × 40 × 40 mm^3) to control the gas composition (Figure 1c). A 7.5 kV peak-to-peak sinusoidal voltage at 50 kHz was applied to the powered electrode, resulting in 6−12 W of power deposited into the plasma, depending on the substrate. See additional electrical characterization details in the Experimental Section. The ignited Ar plasma jet propagated down the tube for 35 mm and then expanded in N_2 at a gap of 5 mm from the substrate such that the diameter of the impinging jet on the substrate was roughly 4 mm.

A typical experiment included in situ substrate temperature measurements using an infrared (IR) camera. To avoid possible interference with IR radiation from the plasma itself, the sample substrate was mounted on a 0.2 mm black tape with an emissivity of 0.92, and the IR camera was directed at the back of the tape. The temperature difference between the front surface and back surface of the substrate was determined to be around 0.6 °C based on both experimental measurements and COMSOL simulations. Note that the camera accuracy is calibrated within ±2 °C or ±2% of the reading. Therefore, the camera measurements at front and back surfaces are within the given uncertainty values, and the back-surface temperatures can effectively approximate the front surface temperature of the substrate. The IR image was calibrated in preliminary tests against a thermocouple mounted on a sample itself, enabling us to deduce sample temperatures from IR images (Figure 1d). The plasma jet was also characterized by optical emission spectroscopy (OES) detecting Ar emission lines showing that the electron temperature in the plasma was approximately 0.79 eV (see Supporting Information S1 for details), consistent with typical values reported for plasma jets.[50]

The plasma jet sintering process consisted of cycles in which the plasma jet was turned on and off periodically. One cycle consisted of an active plasma time (30 s) followed by a cooling time (30 s), for a duty cycle of 50%. To achieve uniform sintering across the printed film, we printed 2 × 2 mm^2 thin films (Figure 1b) that were entirely covered by the plasma jet impinging on the surface. Aerosol jet printed silver NP films were printed with a single pass, and the printing parameters are presented in Table S1 of Supporting Information.

As illustrated in Figure 1e,f, the low-temperature nature of the plasma sintering process enabled printing and sintering on highly delicate substrates, such as plastics, or even biomaterials such as leaves and tomatoes. Figure 1g,h shows scanning electron microscopy (SEM) images of the silver NP films before and after plasma sintering for 100 min, illustrating that the plasma effectively densifies particles, which is the key for obtaining conductive films.

Under periodic plasma jet operation, the electrical resistance of the printed film was reduced over 6 orders of magnitude in the first 20 min of plasma exposure, as shown in Figure 2, and then continued to decrease by another order of magnitude over 80 min, plateauing at a final value. The initial rapid drop in the sheet resistance is likely due to the removal of surfactants in the ink by energetic plasma ions and electrons that dissociate chemical stabilizers. Energy-dispersive X-ray (EDX) analysis revealed an almost 50% decrease in carbon mass after 20 min of pulsed operation, which can be correlated to the removal of organic compounds (Table S2 in Supporting Information).

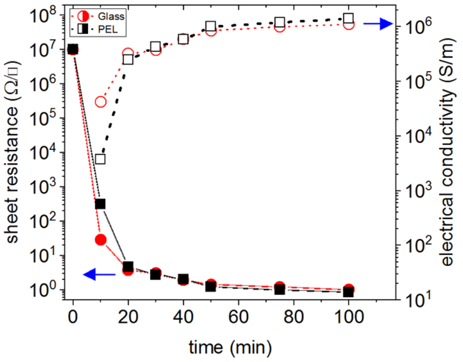

Figure 2. Sheet resistance (left axis) and electrical conductivity (right axis) of printed silver NP films as a function of plasma sintering time for glass and PEL paper substrates. Repeatability was assessed as described in the Experimental Section.

The corresponding electrical conductivity of the printed silver films continuously increased as the sintering time progressed, achieving a maximum electrical conductivity of 1.1 × 10^6 and 1.4 × 10^6 S/m for films printed on glass and PEL respectively. We attribute this slightly higher electrical conductivity on PEL to the porosity of the PEL paper. It is known that nonthermal plasmas can propagate through porous media via both surface ionization waves and microfilaments,[51−54] and thus, the plasma jet likely penetrates into the PEL, allowing for greater exposure to the silver NPs. It is notable that the measured conductivity values are lower than bulk silver conductivity (6.3 × 10^7 S/m[55]), suggesting that the films were not fully sintered. However, conductivity values ~10^6 S/m are comparable to other plasma-based techniques (see Table 1).

Sintering occurs by NPs constructing bridges at their grain boundaries facilitating mass transport and eventually forming a continuous medium leading to enhanced electrical conductivity. Figure 3 shows densification of silver NPs on both glass and PEL paper. While the NPs generally preserved their shapes on the glass substrate, a more dispersed appearance and potentially redeposited particles were observed after 100 min of operation. Conceivably, films on glass experienced a structural transition between 50 and 100 min of operation that led to larger NP clusters and distributed atoms on top of them. In contrast, films on PEL paper formed structures filling the gaps between NPs after 20 min and advanced to a fully continuous medium after 100 min, possibly due to the porous nature of the substrate permitting penetrating energy transfer from the plasma propagating through the pores. SEM images show that the sintering procedure on different substrates may undergo different densification mechanisms over time.

The temperature variation on both the glass and PEL substrates during plasma on and off periods was captured with the IR camera. Figure 4a shows the temperature rising and falling with the corresponding plasma on/off periods for the first 10 cycles. The maximum temperature on glass stayed

Table 1. Comparison of Different Argon Plasma Sintering Conditions for Silver NP Films on Various Substrates

plasma application	plasma power (W)	particle size (nm)	film thickness (μm)	process time	electrical conductivity (S/m)	maximum operation temperature (°C)	refs
low pressure Ar plasma	900	23	1	60 min	1.14×10^7	150	Ma, et al. 2014[25]
		77			5.35×10^6		
low pressure Ar plasma	300	5−12 nm	0.5	30 min (pre-drying at 100 °C for 60 min)	1.89×10^7	100	Pabst, et al. 2013[60]
		30−50 nm	1.8				
low pressure Ar plasma	300	20−30 nm	0.18	60 min	1.85×10^7	70	Wolf, et al. 2013[61]
atm pressure Ar plasma pencil	<20	5−10 nm	0.9	2 min (150 cycles)	3.94×10^6	60	Wünscher, et al. 2012[59]
		30−50 nm	0.36		6.21×10^6		
atm pressure Ar plasma jet	6	30−50 nm	0.86	50 min (50 cycles)	1.00×10^6	48	this work

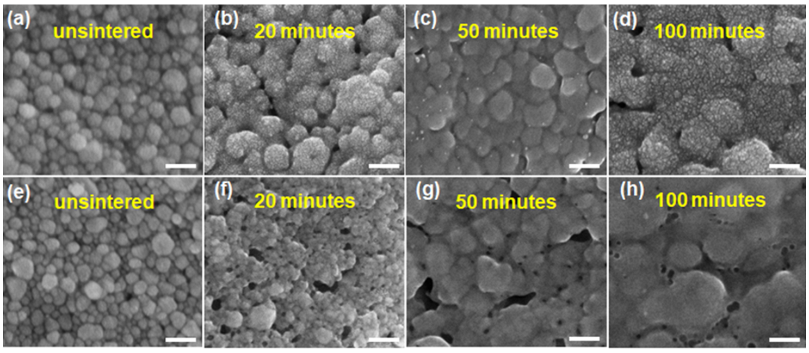

Figure 3. Top-view SEM images of (a−d) unsintered and plasma sintered silver films on glass and (e−h) unsintered and plasma sintered Ag NP films on PEL paper. Scale bars are 50 nm.

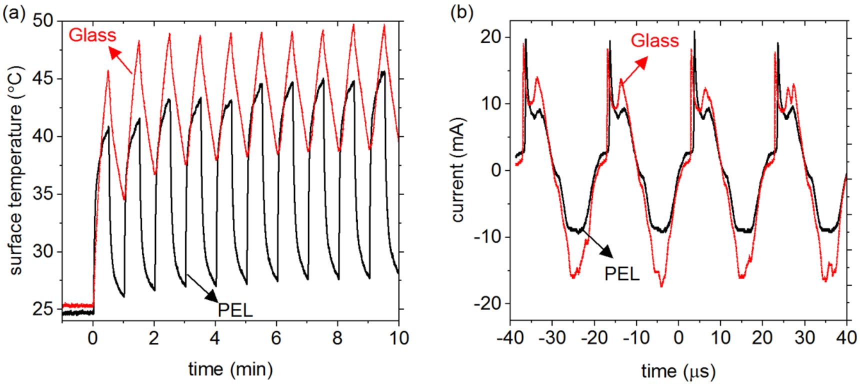

Figure 4. (a) Maximum surface temperature during sintering with cyclic plasma on and off periods (30 s on/off) on glass and PEL paper. The IR camera has an uncertainty of ±2%. (b) Sinusoidal plasma current measured during the plasma on period of a single cycle for an applied peak-to-peak voltage of 7.5 kV at 50 kHz.

below 50 °C, while the thinner PEL paper diffused the heat away more effectively during the cooling period, resulting in lower maximum temperature around 45 °C. Since this is not primarily a thermal process, it is likely that the cooling down time during the plasma-off portion of the cycle does not affect sintering or the conductivity considerably. However, the potential effect of relocation of atoms through necking growth driven by capillary pressure during the plasma-off time cannot be ruled out.[56]

To confirm that the low-temperature plasma sintering process was not thermally driven, two control tests were conducted by thermally processing similarly printed samples in an Ar oven. A maximum electrical conductivity of 2.65 ± 0.33 × 10^7 S/m (42% of bulk silver[55]) was achieved for a thermally sintered film at 300 °C for 2 h. On the contrary, thermally processed films at 50 °C for 100 min were nonconductive, which supports the conclusion that plasma sintering activates the NP ink nonthermally, illustrating its potential for low-temperature surface functionalization applications.

The plasma jet enabled sintering into the submicron film thickness, with effective energy transfer from plasma species to surface NPs propagating to deeper layers. Figure S2 in Supporting Information shows cross-sectional analysis of films on both substrates. A silver film on glass demonstrated interconnected NP islands up to 20% of the entire thickness from the top layer toward the bottom after sintering. For the

PEL substrates, almost the entire film transformed into a unified new phase with larger clusters that were denser at the top layers. After 100 min of sintering, wavy structures on the top surface and a thickness reduction of 4−5% were observed. This deeper penetration of the sintering likely led to achieving a higher conductivity value on PEL paper than on glass.

For both substrates, we generated the plasma jet using an applied sinusoidal voltage of 7.5 ± 0.7 kV at 50 kHz to the powered electrode. Notably, the plasma power for the glass substrates was calculated to be 11.7 ± 0.2 W, whereas the power for films on PEL substrates was 6.1 ± 0.6 W. We attribute this difference in power to the electrical permittivity of the two substrates ($\varepsilon_{\text{glass}} = 11.4$, $\varepsilon_{\text{PEL}} = 1.5$), which in turn affects surface ionization wave propagation for impinging plasma jets.[38,57,58] Surfaces with a larger dielectric permittivity drop more voltage across the plasma column, while surfaces with a smaller permittivity more effectively enable lateral expansion of the plasma jet on the surface as surface ionization waves, until the ionization waves quench due to a lack of accumulated charges. The change in plasma properties was also evident in the plasma current traces, as observed in Figure 4b. The current during the negative half-cycle was substantially higher on glass compared to PEL paper, resulting in the higher deposited power for glass substrates.

Plasma jets and similar nonthermal plasmas have emerged as promising candidates for roll-to-roll processing of value-added materials.[1,2] In terms of applying nonthermal plasmas to sintering, a number of studies have explored low pressure Ar plasmas. Compared to these, our plasma jet provides a significant reduction in power and operating temperature while also enabling atmospheric pressure processing (Table 1), which reduces complexity, time, and cost. We note that an atmospheric pressure plasma pencil study achieved comparable electrical conductivity values to those we report here, while improving the film conductivity by 2 orders of magnitude in 2 min.[28,59] While the 2 min was remarkably fast, their initial conductivity, prior to sintering, was orders of magnitudes higher than ours, possibly due to their ink formulation and particle size. Our plasma jet also increases the conductivity by 2 orders of magnitude in the first few minutes, which we attribute primarily to surfactant removal. We note that the plasma sintering results shown in Table 1 are comparable to other, primarily chemical, low-temperature sintering methods.[30−33] One advantage of the plasma jet is that it is a localized process (as shown in Figure 1) and thus offers the potential for scanned sintering to produce graded conductivities, which cannot be achieved with purely chemical low-temperature sintering.

We have also applied this plasma jet sintering approach to highly curved and delicate substrates. As shown in Figure 5, a continuous Ar plasma jet with a power of 3 W can successfully sinter silver NP films on a tomato without any damage to its surface. Note that the initial data point with the highest sheet resistance shows that the film was not conductive prior to sintering. We measured unsintered samples with a two-point probe multimeter, and the resistance values were above the measurable scale of our multimeter for all samples. Therefore, the first point (at 0 min) is an artificial representation of a nonconductive sample. Figure 5a shows the printed silver film on a tomato before sintering, and Figure 5b shows the sintered film after 45 min. Moreover, ambient temperature plasma sintering can be used for sintering printed pattern on low-melting-temperature substrates such as PDMS or silicone (Figure 5c). Note that sintering conditions in Figure 5c showing a pattern on silicone wrapped around a finger do not contain a direct risk to human subject. Figure 5d shows high-resolution printing capabilities on a grape's surface.

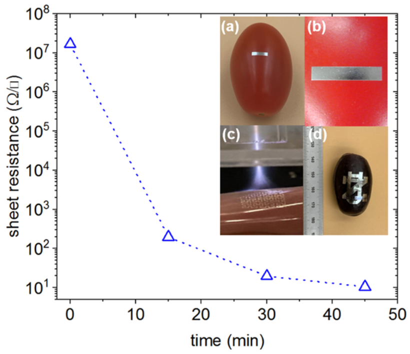

Figure 5. Sheet resistance of the printed silver NP film on a tomato. Insets show (a) printed silver film (1 × 5 mm^2) before sintering, (b) surface of the tomato after sintering, (c) printed pattern on a silicone substrate attached to human skin during plasma sintering, and (d) aerosol jet printed University of Notre Dame logo (interlocking ND) on a grape. The initial data point at 0 min reflects the upper limit of the multimeter and is only included in the figure to convey the magnitude of improvement in resistance after sintering.

3. CONCLUSIONS

We have developed a low-temperature plasma jet process to sinter aerosol jet printed silver NP films. An argon plasma jet facilitated the removal of the surfactants surrounding the NPs and redistributed and densified the remaining particles. The printed NP films achieved a conductivity of 1.4 × 10^6 S/m under ambient plasma operation. Continuously cycling the plasma jet on and off for 30 s allowed us to control the substrate temperature below 50 °C. Operating the plasma jet at a lower power (3 W) enabled sintering of printed structures on delicate substrates such as tomatoes and human skin under continuous operation, confirming the feasibility of room-temperature plasmas for processing electronics on biomaterials. While the achieved electrical conductivities were not as high as conventional sintering or the bulk material, it is likely that sintering is a strong function of the plasma power, as is the substrate temperature. There is therefore a trade-off between sintering performance and substrate temperature. Still, these results show that nonthermal plasma jet sintering has the potential to facilitate manufacturing processes for flexible electronic applications on temperature-sensitive components. Future work by integrating the plasma jet and printing process holds promise in advancing printing and in situ sintering for scalable and low-cost additive manufacturing.

4. EXPERIMENTAL SECTION

4.1. Aerosol Jet Printing of Silver NPs.

Silver NP films were printed using an aerosol jet printer (AJ 300 system, Optomec, Inc., Albuquerque, NM). Clariant's PRELECT TPS nanosilver conductive ink with 30−50 nm NPs was diluted with DI water at a ratio of 1:2.5 (ink to water), followed by batch sonication for 30 min. The average silver NP size was 30−50 nm, and the ink contained ethylene glycol with 50% solid content. The density, viscosity, and surface tension of the ink were 1.8 g/mL, 25 ± 2 mPa s, and 35 ± 3 mN/m, respectively. Prior to printing, an AutoCAD schematic design of the pattern was loaded onto the printer to generate a toolpath for printing. An ultrasonic atomizer created a mist of droplets with a size range of ~1−5 μm that were directed by a carrier gas (N_2) and deposited onto the substrate. Table S1 in Supporting Information presents the printing parameters. We used glass slides (VWR plain and frosted microslides, USA) with a thickness of 1 mm and PEL P60 paper (Printed Electronics Ltd., UK) with a thickness of ∼0.1 mm as substrates. Before printing, the glass slides were first washed with deionized water and isopropyl alcohol, followed by O_2 plasma treatment for 7 min (Harrick Plasma, PDC-001-HP (115 V)/PDC-002-HP (230 V), New York, USA).

4.2. Characterization. *4.2.1. Plasma Generation and Characterization.* The applied sinusoidal voltage was controlled using a transformer (CMI-5533) and a power amplifier (Powertron, model 50A, RF Amplifier), and the frequency was set using a function generator (Agilent 33220A). The frequency can be varied between 50 and 100 kHz, and the applied peak-to-peak voltage to the entire circuit ranged from 5 to 8 kV. The applied voltage was measured using a high-voltage probe (Tektronix P6015A) and monitored on a digital oscilloscope (Tektronix TBS 2000) with a time resolution of 2 ns. The current trace was recorded across an external resistor (R_x) of 10 kΩ. Charge accumulation was measured across a capacitor C_x (2.2 nF). Oscilloscope data were extracted with 8-bit resolution and a sampling rate of 250 MS/s. The average deposited power to the plasma was calculated via

$$P = \frac{1}{T}\int_0^T V_1(t)I(t)\mathrm{d}t - \frac{1}{2}\frac{V_2^{\ 2}}{R_x} \quad (1)$$

where T is the period of one sinusoidal cycle, V_1 is the total applied voltage, V_2 is the voltage across the resistor, and I is the total current. OES was conducted with a Shamrock 303i Andor spectrometer with 0.1 nm wavelength resolution and a high-speed Andor iStar Intensified CMOS camera.

4.2.2. Thermal Characterization. A FLIR T420 IR camera was utilized to measure the spatiotemporal evolution of the surface temperature on the back side of substrates. The camera has a thermal sensitivity of < 0.045 °C at 30 °C with an accuracy of 2%.

4.2.3. Electrical Resistivity Characterization. Silver NP films were printed in square patterns (2×2 mm^2) with four pads on the corners to connect copper leads for electrical conductivity measurements using the van der Pauw method. The electrical leads were connected to the printed film using silver paint (Flash-dry silver conductive paint, SPI, USA). After measuring the sheet resistance, the thickness of each film was measured at five different locations using a 2D profilometer (DektakXT, Bruker, USA). The reported conductivities are the average value of five measurements with a corresponding uncertainty of 3% that is calculated using the Student's t distribution at 95% confidence for all values. Repeatability was assessed by conducting a series of tests for different sintering times ($N = 3$ at each time) under slightly different conditions (4000 sccm of Ar and 10 sccm of N_2 in the environment, yielding 4.5 W and 7.5 W for PEL and glass substrates, respectively) and determining the coefficient of variation for the measured sheet resistance (see Figure S3). The coefficient of variation for the sheet resistance ranged from 73 to 62% for glass and PEL substrates, for 20 min time due to partial sintering, to 8 and 20%, respectively, for 75 min when the film was fully sintered.

4.2.4. Scanning Electron Microscopy. A scanning electron microscope (Helios G4 Ux DualBeam (FEI), USA), with a working voltage of 15 kV and a working distance of 4.5 mm, was used for top-view and cross-sectional imaging of the printed silver NP films.

■ ASSOCIATED CONTENT

Supporting Information

The Supporting Information is available free of charge at https://pubs.acs.org/doi/10.1021/acsami.1c14049.

> OES of argon (Ar) plasma jets; cross-sectional SEM images of thin films; AJP conditions; EDX spectroscopy analysis of unsintered and sintered films; and coefficient of variation for the measured sheet resistance (PDF)

■ AUTHOR INFORMATION

Corresponding Authors

Yanliang Zhang − *Department of Aerospace and Mechanical Engineering, University of Notre Dame, Notre Dame, Indiana 46556, United States;* orcid.org/0000-0001-7423-8001; Email: yzhang45@nd.edu

David B. Go − *Department of Aerospace and Mechanical Engineering, University of Notre Dame, Notre Dame, Indiana 46556, United States; Department of Chemical and Biomolecular Engineering, University of Notre Dame, Notre Dame, Indiana 46556, United States;* orcid.org/0000-0001-8948-1442; Email: dgo@nd.edu

Authors

Nazli Turan − *Department of Aerospace and Mechanical Engineering, University of Notre Dame, Notre Dame, Indiana 46556, United States;* orcid.org/0000-0002-1915-3125

Mortaza Saeidi-Javash − *Department of Aerospace and Mechanical Engineering, University of Notre Dame, Notre Dame, Indiana 46556, United States*

Jiahao Chen − *Department of Aerospace and Mechanical Engineering, University of Notre Dame, Notre Dame, Indiana 46556, United States*

Minxiang Zeng − *Department of Aerospace and Mechanical Engineering, University of Notre Dame, Notre Dame, Indiana 46556, United States;* orcid.org/0000-0002-3513-9200

Complete contact information is available at: https://pubs.acs.org/10.1021/acsami.1c14049

Author Contributions

§N.T. and M.S.-J. contributed equally to this work.

Notes

The authors declare no competing financial interest.

■ ACKNOWLEDGMENTS

This material is based upon work supported by the US Air Force Office of Scientific Research under Award no. FA9550-18-1-0157, the Department of Energy under Award no. DE-EE0009103, and the National Science Foundation under award CMMI-1747685. N.T. and D.B.G. thank Jinyu Yang for assistance with the OES analysis.

■ REFERENCES

(1) Niittynen, J.; Abbel, R.; Mäntysalo, M.; Perelaer, J.; Schubert, U. S.; Lupo, D. Alternative Sintering Methods Compared to Conventional Thermal Sintering for Inkjet Printed Silver Nanoparticle Ink. *Thin Solid Films* **2014**, *556*, 452−459.

(2) Kamyshny, A.; Magdassi, S. Conductive Nanomaterials for 2D and 3D Printed Flexible Electronics. *Chem. Soc. Rev.* **2019**, *48*, 1712−1740.

(3) Khan, S.; Lorenzelli, L.; Dahiya, R. S. Technologies for Printing Sensors and Electronics Over Large Flexible Substrates: A Review. *IEEE Sens. J.* **2015**, *15*, 3164−3185.

(4) Saeidi-Javash, M.; Kuang, W.; Dun, C.; Zhang, Y. 3D Conformal Printing and Photonic Sintering of High-Performance Flexible Thermoelectric Films Using 2D Nanoplates. *Adv. Funct. Mater.* **2019**, *29*, 1901930.

(5) Zeng, M.; Kuang, W.; Khan, I.; Huang, D.; Du, Y.; Saeidi-Javash, M.; Zhang, L.; Cheng, Z.; Hoffman, A. J.; Zhang, Y. Colloidal Nanosurfactants for 3D Conformal Printing of 2D van Der Waals Materials. *Adv. Mater.* **2020**, *32*, 2003081.

(6) Tsumaki, M.; Nitta, K.; Jeon, S.; Terashima, K.; Ito, T. Development of Plasma-Assisted Inkjet Printing and Demonstration

for Direct Printing of Conductive Silver Line. *J. Phys. D: Appl. Phys.* **2018**, *51*, 30LT01.

(7) Bodla, K. K.; Garimella, S. V. Simulated Microstructural Evolution and Design of Porous Sintered Wicks. *J. Heat Transfer* **2014**, *136*, 072601.

(8) German, R. M. *Sintering: From Empirical Observations to Scientific Principles*; Butterworth-Heinemann, 2014; pp 13−40.

(9) Wilkes, C. E.; Summers, J. W.; Daniels, C. A.; Berard, M. T. *PVC Handbook*; : Munich, Cincinnati, 2005; p 414.

(10) Danaei, R.; Varghese, T.; Ahmadzadeh, M.; McCloy, J.; Hollar, C.; Sadeq Saleh, M.; Park, J.; Zhang, Y.; Panat, R. Ultrafast Fabrication of Thermoelectric Films by Pulsed Light Sintering of Colloidal Nanoparticles on Flexible and Rigid Substrates. *Adv. Eng. Mater.* **2019**, *21*, 1800800.

(11) Liu, W.; An, R.; Wang, C.; Zheng, Z.; Tian, Y.; Xu, R.; Wang, Z. Recent Progress in Rapid Sintering of Nanosilver for Electronics Applications. *Micromachines* **2018**, *9*, 346.

(12) Chiu, W.-T.; Chen, C.-L.; Chen, Y.-Y. A Strategy to Optimize the Thermoelectric Performance in a Spark Plasma Sintering Process. *Sci. Rep.* **2016**, *6*, 23143.

(13) Cahill, J. T.; Vasquez, V. R.; Misture, S. T.; Edwards, D.; Graeve, O. A. Effect of Current on Diffusivity in Metal Hexaborides: A Spark Plasma Sintering Study. *ACS Appl. Mater. Interfaces* **2017**, *9*, 37357−37363.

(14) Roy, P.; Pal, V.; Maiti, T. Effect of Spark Plasma Sintering (SPS) on the Thermoelectric Properties of SrTiO3:15 At% Nb. *Ceram. Int.* **2017**, *43*, 12809−12813.

(15) Hitchcock, D.; Livingston, R.; Liebenberg, D. Improved Understanding of the Spark Plasma Sintering Process. *J. Appl. Phys.* **2015**, *117*, 174505.

(16) Joos, M.; Cerretti, G.; Veremchuk, I.; Hofmann, P.; Frerichs, H.; Anjum, D. H.; Reich, T.; Lieberwirth, I.; Panthöfer, M.; Zeier, W. G.; Tremel, W. Spark Plasma Sintering (SPS)-Assisted Synthesis and Thermoelectric Characterization of Magnéli Phase V_6O_{11}. *Inorg. Chem.* **2018**, *57*, 1259−1268.

(17) Alayli, N.; Schoenstein, F.; Girard, A.; Tan, K. L.; Dahoo, P. R. Spark Plasma Sintering Constrained Process Parameters of Sintered Silver Paste for Connection in Power Electronic Modules: Microstructure, Mechanical and Thermal Properties. *Mater. Chem. Phys.* **2014**, *148*, 125−133.

(18) Yadhukulakrishnan, G. B.; Karumuri, S.; Rahman, A.; Singh, R. P.; Kaan Kalkan, A.; Harimkar, S. P. Spark Plasma Sintering of Graphene Reinforced Zirconium Diboride Ultra-High Temperature Ceramic Composites. *Ceram. Int.* **2013**, *39*, 6637−6646.

(19) Nieto, A.; Lahiri, D.; Agarwal, A. Synthesis and Properties of Bulk Graphene Nanoplatelets Consolidated by Spark Plasma Sintering. *Carbon* **2012**, *50*, 4068−4077.

(20) Munir, Z. A.; Anselmi-Tamburini, U.; Ohyanagi, M. The Effect of Electric Field and Pressure on the Synthesis and Consolidation of Materials: A Review of the Spark Plasma Sintering Method. *J. Mater. Sci.* **2006**, *41*, 763−777.

(21) Tyagi, K.; Gahtori, B.; Bathula, S.; Toutam, V.; Sharma, S.; Singh, N. K.; Dhar, A. Thermoelectric and Mechanical Properties of Spark Plasma Sintered Cu_3SbSe_3 and Cu_3SbSe_4: Promising Thermoelectric Materials. *Appl. Phys. Lett.* **2014**, *105*, 261902.

(22) Li, X. Y.; Chen, L. D.; Fan, J. F.; Zhang, W. B.; Kawahara, T.; Hirai, T. Thermoelectric Properties of Te-Doped CoSb3 by Spark Plasma Sintering. *J. Appl. Phys.* **2005**, *98*, 083702.

(23) Bruggeman, P.; Brandenburg, R. Atmospheric Pressure Discharge Filaments and Microplasmas: Physics, Chemistry and Diagnostics. *J. Phys. D: Appl. Phys.* **2013**, *46*, 464001.

(24) Go, D. B. *Ionization and Ion Transport*; Morgan & Claypool Publishers, 2018.

(25) Ma, S.; Bromberg, V.; Liu, L.; Egitto, F. D.; Chiarot, P. R.; Singler, T. J. Low Temperature Plasma Sintering of Silver Nanoparticles. *Appl. Surf. Sci.* **2014**, *293*, 207−215.

(26) Renn, M. Method and Apparatus for Low-Temperature Plasma Sintering. U.S. Patent 20,070,154,634 A1, 2007.

(27) Reinhold, I.; Hendriks, C. E.; Eckardt, R.; Kranenburg, J. M.; Perelaer, J.; Baumann, R. R.; Schubert, U. S. Argon Plasma Sintering of Inkjet Printed Silver Tracks on Polymer Substrates. *J. Mater. Chem.* **2009**, *19*, 3384.

(28) Wünscher, S.; Abbel, R.; Perelaer, J.; Schubert, U. S. Progress of Alternative Sintering Approaches of Inkjet-Printed Metal Inks and Their Application for Manufacturing of Flexible Electronic Devices. *J. Mater. Chem. C* **2014**, *2*, 10232−10261.

(29) Wünscher, S.; Stumpf, S.; Perelaer, J.; Schubert, U. S. Towards Single-Pass Plasma Sintering: Temperature Influence of Atmospheric Pressure Plasma Sintering of Silver Nanoparticle Ink. *J. Mater. Chem. C* **2014**, *2*, 1642.

(30) Mo, L.; Guo, Z.; Wang, Z.; Yang, L.; Fang, Y.; Xin, Z.; Li, X.; Chen, Y.; Cao, M.; Zhang, Q.; Li, L. Nano-Silver Ink of High Conductivity and Low Sintering Temperature for Paper Electronics. *Nanoscale Res. Lett.* **2019**, *14*, 197.

(31) Magdassi, S.; Grouchko, M.; Berezin, O.; Kamyshny, A. Triggering the Sintering of Silver Nanoparticles at Room Temperature. *ACS Nano* **2010**, *4*, 1943−1948.

(32) Tang, Y.; He, W.; Zhou, G.; Wang, S.; Yang, X.; Tao, Z.; Zhou, J. A New Approach Causing the Patterns Fabricated by Silver Nanoparticles to Be Conductive without Sintering. *Nanotechnology* **2012**, *23*, 355304.

(33) Shen, W.; Zhang, X.; Huang, Q.; Xu, Q.; Song, W. Preparation of Solid Silver Nanoparticles for Inkjet Printed Flexible Electronics with High Conductivity. *Nanoscale* **2014**, *6*, 1622−1628.

(34) Akishev, Y. S.; Karalnik, V. B.; Medvedev, M. A.; Petryakov, A. V.; Trushkin, N. I.; Shafikov, A. G. How Ionization Waves (Plasma Bullets) in Helium Plasma Jet Interact with a Dielectric and Metallic Substrate. *J. Phys.: Conf. Ser.* **2017**, *927*, 012040.

(35) Fanelli, F.; Fracassi, F. Atmospheric Pressure Non-Equilibrium Plasma Jet Technology: General Features, Specificities and Applications in Surface Processing of Materials. *Surf. Coat. Technol.* **2017**, *322*, 174−201.

(36) Gaens, W. V.; Bogaerts, A. Kinetic Modelling for an Atmospheric Pressure Argon Plasma Jet in Humid Air. *J. Phys. D: Appl. Phys.* **2013**, *46*, 275201.

(37) Hofmann, S.; van Gessel, A. F. H.; Verreycken, T.; Bruggeman, P. Power Dissipation, Gas Temperatures and Electron Densities of Cold Atmospheric Pressure Helium and Argon RF Plasma Jets. *Plasma Sources Sci. Technol.* **2011**, *20*, 065010.

(38) Klarenaar, B. L. M.; Guaitella, O.; Engeln, R.; Sobota, A. How Dielectric, Metallic and Liquid Targets Influence the Evolution of Electron Properties in a Pulsed He Jet Measured by Thomson and Raman Scattering. *Plasma Sources Sci. Technol.* **2018**, *27*, 085004.

(39) Johnson, M. J.; Boris, D. R.; Petrova, T. B.; Walton, S. G. Spatio-Temporal Characterization of a Pulsed DC Atmospheric Pressure Plasma Jet Interacting with Substrates. *J. Phys. D: Appl. Phys.* **2020**, *54*, 085202.

(40) Laroussi, M. Plasma Medicine: A Brief Introduction. *Plasma* **2018**, *1*, 47−60.

(41) Laroussi, M. Low Temperature Plasma Jets: Characterization and Biomedical Applications. *Plasma* **2020**, *3*, 54−58.

(42) Boekema, B. K. H. L.; Vlig, M.; Guijt, D.; Hijnen, K.; Hofmann, S.; Smits, P.; Sobota, A.; van Veldhuizen, E. M.; Bruggeman, P.; Middelkoop, E. A New Flexible DBD Device for Treating Infected Wounds: *In Vitro* and *Ex Vivo* Evaluation and Comparison with a RF Argon Plasma Jet. *J. Phys. D: Appl. Phys.* **2016**, *49*, 044001.

(43) Urabe, K.; Shirai, N.; Tomita, K.; Akiyama, T.; Murakami, T. Diagnostics of Atmospheric-Pressure Pulsed-Dc Discharge with Metal and Liquid Anodes by Multiple Laser-Aided Methods. *Plasma Sources Sci. Technol.* **2016**, *25*, 045004.

(44) Chen, G.; Hu, W.; Yu, J.; Chen, W.; Huang, J. Exploring the Cooperation Effect of DBD Byproducts and Ag/TiO_2 Catalyst for Water Treatment in an APPJ System. *Plasma Sci. Technol.* **2017**, *19*, 015503.

(45) Mouele, E. S. M.; Tijani, J. O.; Fatoba, O. O.; Petrik, L. F. Degradation of Organic Pollutants and Microorganisms from Wastewater Using Different Dielectric Barrier Discharge Config-

urations—a Critical Review. *Environ. Sci. Pollut. Res.* **2015**, *22*, 18345−18362.

(46) Barni, R.; Biganzoli, I.; Tassetti, D.; Riccardi, C. Characterization of a Plasma Jet Produced by Spark Discharges in Argon Air Mixtures at Atmospheric Pressure. *Plasma Chem. Plasma Process.* **2014**, *34*, 1415−1431.

(47) Yang, J.; Im, S.-K.; Go, D. B. Time-Resolved Characterization of a Free Plasma Jet Formed off the Surface of a Piezoelectric Crystal. *Plasma Sources Sci. Technol.* **2020**, *29*, 045016.

(48) Feng, B. W.; Zhong, X. X.; Zhang, Q.; Chen, Y. F.; Sheng, Z. M.; Ostrikov, K. Size and Electron Density of Open-Air Plasmas Diagnosed by Optical Imaging. *J. Phys. D: Appl. Phys.* **2019**, *52*, 265203.

(49) Lu, X.; Reuter, S.; Laroussi, M.; Liu, D. *Nonequilibrium Atmospheric Pressure Plasma Jets: Fundamentals, Diagnostics, and Medical Applications*; CRC Press, Taylor & Francis Group: Boca Raton, 2019; pp 271−306.

(50) Taghizadeh, L.; Nikiforov, A.; Morent, R.; van der Mullen, J.; Leys, C. Determination of the Electron Temperature of Atmospheric Pressure Argon Plasmas by Absolute Line Intensities and a Collisional Radiative Model: Determination of the Electron Temperature of Atmospheric Pressure. *Plasma Processes Polym.* **2014**, *11*, 777−786.

(51) Zhang, Y.-R.; Neyts, E. C.; Bogaerts, A. Enhancement of Plasma Generation in Catalyst Pores with Different Shapes. *Plasma Sources Sci. Technol.* **2018**, *27*, 055008.

(52) Mujahid, Z.-u. -I.; Kruszelnicki, J.; Hala, A.; Kushner, M. J. Formation of Surface Ionization Waves in a Plasma Enhanced Packed Bed Reactor for Catalysis Applications. *Chem. Eng. J.* **2020**, *382*, 123038.

(53) Cheng, H.; Ma, M.; Zhang, Y.; Liu, D.; Lu, X. The Plasma Enhanced Surface Reactions in a Packed Bed Dielectric Barrier Discharge Reactor. *J. Phys. D: Appl. Phys.* **2020**, *53*, 144001.

(54) Engeling, K. W.; Kruszelnicki, J.; Kushner, M. J.; Foster, J. E. Time-Resolved Evolution of Micro-Discharges, Surface Ionization Waves and Plasma Propagation in a Two-Dimensional Packed Bed Reactor. *Plasma Sources Sci. Technol.* **2018**, *27*, 085002.

(55) Matula, R. A. Electrical Resistivity of Copper, Gold, Palladium, and Silver. *J. Phys. Chem. Ref. Data* **1979**, *8*, 1147−1298.

(56) Kang, S.-J. L. *Sintering: Densification, Grain Growth, and Microstructure*; Materials Science & Engineering; Elsevier: Amsterdam, 2005; pp 12−18.

(57) Norberg, S. A.; Johnsen, E.; Kushner, M. J. Helium Atmospheric Pressure Plasma Jets Touching Dielectric and Metal Surfaces. *J. Appl. Phys.* **2015**, *118*, 013301.

(58) Guaitella, O.; Sobota, A. The Impingement of a KHz Helium Atmospheric Pressure Plasma Jet on a Dielectric Surface. *J. Phys. D: Appl. Phys.* **2015**, *48*, 255202.

(59) Wünscher, S.; Stumpf, S.; Teichler, A.; Pabst, O.; Perelaer, J.; Beckert, E.; Schubert, U. S. Localized Atmospheric Plasma Sintering of Inkjet Printed Silver Nanoparticles. *J. Mater. Chem.* **2012**, *22*, 24569.

(60) Pabst, O.; Perelaer, J.; Beckert, E.; Schubert, U. S.; Eberhardt, R.; Tünnermann, A. All Inkjet-Printed Piezoelectric Polymer Actuators: Characterization and Applications for Micropumps in Lab-on-a-Chip Systems. *Org. Electron.* **2013**, *14*, 3423−3429.

(61) Wolf, F. M.; Perelaer, J.; Stumpf, S.; Bollen, D.; Kriebel, F.; Schubert, U. S. Rapid Low-Pressure Plasma Sintering of Inkjet-Printed Silver Nanoparticles for RFID Antennas. *J. Mater. Res.* **2013**, *28*, 1254−1261.